

HIGH-GRADIENT COBALT NANOMAGNETS ON CANTILEVERS USED TO SENSITIVELY DETECT NUCLEAR MAGNETIC RESONANCE

5.1 Introduction

In the most sensitive MRFM experiments to date, signal has been detected as a force variance generated by interactions between the magnetic field gradient produced by a nanomagnet and magnetic dipole fluctuations in a small ensemble of nuclear spins [12]. An attonewton-sensitivity cantilever is used as the force sensor to detect this interaction. In this limit where the force variance is measured, for a given cantilever sensitivity and imaging resolution, the signal acquisition time is dependent on the magnetic tip-field gradient such that the acquisition time is proportional to the inverse of the field gradient to the fourth power [48]. To achieve high-sensitivity MRFM detection, it is thus critical to use a high gradient magnetic tip.

The highest-gradient nanomagnets used in MRFM experiments to date have been fabricated on flat substrates [12, 48] and the samples that were studied were adhered to the leading edges of the high-compliance cantilevers. As we transition from robust, small samples, such as the tobacco mosaic virus studied by high-resolution nuclear magnetic resonance (NMR) MRFM imaging in Ref. 12, to instead working with large-area samples or delicate biomacromolecules that require vitrification to be studied at cryogenic temperatures, it will be critical to have the flat substrate available for sample preparation.

Prior MRFM studies that have used the “magnet-on-cantilever” geometry [25, 30, 51–56] have either used micrometer-scale magnetic particles or have reduced the dimensions of large magnetic particles by ion beam milling, which incurred damage due to ion implanta-

tion. In practice these tips produced a gradient nearly an order of magnitude smaller than that achieved by Degen and co-workers. Thus nearly 10^4 longer imaging times would be required to achieve the 4 to 10 nm resolution of Ref. 12 using the best ion-beam milled tip demonstrated to date.

In this chapter, magnet-on-cantilever detection of NMR was achieved using an attonewton-sensitivity cantilever with an integrated cobalt nanomagnet-tipped silicon chip (Section 3.6). The observed magnetic tip-field gradient exceeds previous gradients produced by magnets on cantilevers by at least a factor of eight [25, 53, 54, 56, 57]. Remarkably, the tip gradient is comparable to the tip employed in the high-resolution imaging experiment of Ref. 12. These results thus demonstrate the potential for achieving 4 to 10 nm resolution proton magnetic resonance imaging with reasonable three-dimensional acquisition times for a wide range of thin-film organic samples.

NMR-MRFM signal was measured by using the cobalt nanomagnet-tipped cantilever to detect stochastic proton magnetization from a polystyrene film spun-cast over a microwire [60]. Artifact-free detection of NMR in this magnet-on-cantilever experiment required substantial modification of the spin-modulation protocols of Refs. 56 and 12. The spin signal was studied as a function of radiofrequency (rf) irradiation frequency at multiple tip-sample separations. By modeling this data numerically, the tip field and tip-field gradient were determined. The magnetic integrity of the tip at the nanoscale was assessed by comparing the spin signal to simulations carried out using different damage models. Measurements of force noise as a function of tip-sample separation over a copper microwire and over silicon indicate a larger-than-expected surface noise [81]; methods are suggested for mitigating this surface noise in future experiments.

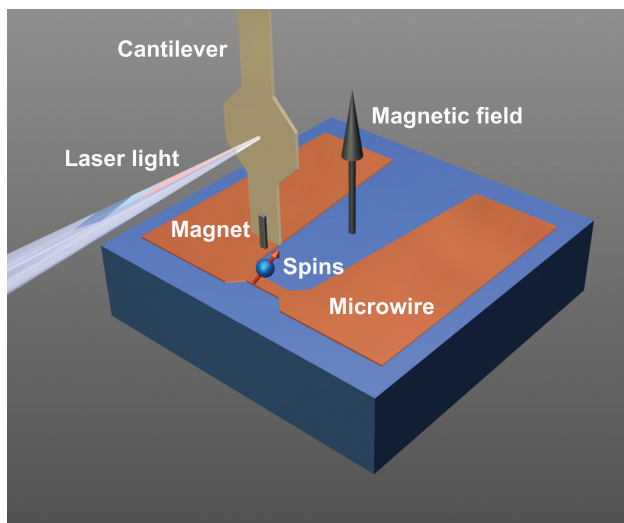


Figure 5.1: Schematic of the experiment. A cobalt magnet with cross section $225 \text{ nm} \times 79 \text{ nm}$ was extended past the leading edge of an attonewton-sensitivity cantilever. The cantilever was centered over a $1 \text{ }\mu\text{m}$ wide microwire coated with 40 nm of polystyrene. An external 2.63 T magnetic field was applied in the direction of the long axis of the cantilever as shown. A laser interferometer was centered on a $30 \text{ }\mu\text{m}$ wide pad to measure cantilever vibrations.

5.2 Experimental Methods

The experiment is illustrated in Figure 5.1.¹ The IBM Almaden Research Center magnetic resonance force microscope used here has been described in detail elsewhere [12, 60]. Measurements were conducted in high vacuum ($P < 10^{-6} \text{ mbar}$) with the temperature maintained at $T = 5.5 \text{ K}$. In all experiments reported here, both the sample and the cantilever were electrically grounded.

5.2.1 Magnet-Tipped Cantilever Characterization

Cobalt nanomagnet-tipped cantilevers (Figure 5.2) were prepared by using the nanomagnet-tipped chip procedure described in Section 3.6 and serially attaching the magnet-tipped

¹Figures 5.1, 5.2, 5.3, 5.4, and 5.5 reprinted with permission from J. G. Longenecker *et al.*, ACS Nano **6**, 9637 (2012). Copyright 2012, American Chemical Society.

chips to attonewton-sensitivity cantilevers using focused ion beam (FIB) manipulation (Section 3.7). The attonewton-sensitivity cantilevers were 4 μm wide, 200 μm long, and had a 30 μm wide reflective pad centered 70 μm from the leading edge (Figure 5.2(c)). The nanomagnets, which were deposited by electron beam (e-beam) evaporation, consisted of a 4.0 ± 0.2 nm thick titanium adhesion layer, 79.2 ± 4.7 nm cobalt layer, and 8.0 ± 0.5 nm platinum capping layer. In order to prevent oxidation of the cobalt magnets, it was critical to not exceed processing temperatures of 115°C once the nanomagnets were evaporated. Scanning electron microscope (SEM) images of the magnet-tipped chip and overhanging magnet are shown in Figure 5.2(a) and Figure 5.2(b), respectively. As seen in Figure 5.2(b), the cobalt nanomagnet extended past the leading edge of the magnet-tipped chip by ~ 300 nm. Magnet-tipped cantilevers were prepared at Cornell University four weeks before they were transferred to the MRFM apparatus at IBM Almaden Research Center. They were exposed to ambient air for approximately five days, were stored under nitrogen for three days, and were otherwise stored under a vacuum of 10^{-4} mbar.

The magnet-tipped cantilever used in this study had a resonance frequency $f_c = 6644\text{Hz}$, an intrinsic quality factor $Q = 8.4 \times 10^4$, and a spring constant $k = 1.0 \text{ mN m}^{-1}$. Cantilever displacement was monitored with a low-power [67], temperature-tuned [145] fiber optic interferometer ($\lambda = 1550 \text{ nm}$, $P \sim 25 \text{ nW}$). The interferometer output was sent to a field programmable gate array (FPGA), which was used to either control the cantilever Q *via* negative feedback [146] or self-oscillate the cantilever to a set amplitude *via* positive feedback [147]. The output of the FPGA drove a piezoelectric disk at the base of the cantilever holder. The cantilever spring constant was determined from the mean square displacement of the undriven cantilever at a temperature $T = 5.5\text{K}$ [138]; a correction factor was used to account for the distance from the reflective pad to the end of the cantilever. Based on the $\pm 15 \mu\text{m}$ uncertainty in the position of the laser, the error in k could be as large as $\pm 40\%$. To study cantilever dissipation, the cantilever ringdown time τ was measured and a cantilever quality

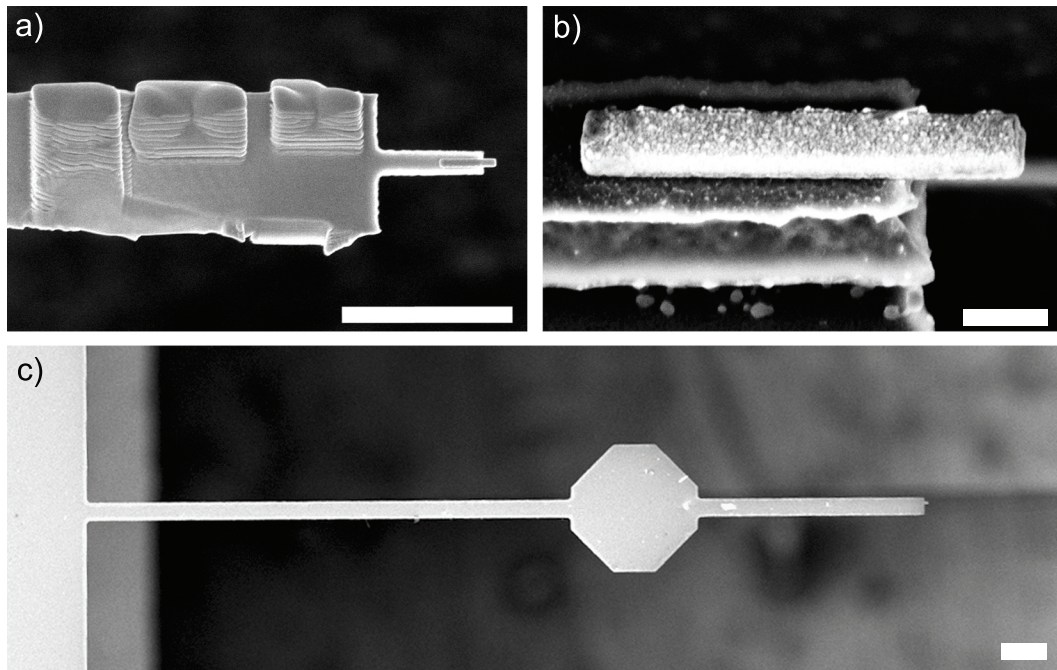


Figure 5.2: SEM images of the magnet-tipped cantilever used in the MRFM experiment. (a) Top-view image of the magnet-tipped chip attached to an underlying cantilever by ion-assisted platinum deposition; three rectangular platinum patches can be seen on the bottom side of the chip. The cobalt magnet is seen to overhang a $3\ \mu\text{m}$ long finger at the leading edge of the chip. Scale bar = $5\ \mu\text{m}$. (b) Angled image of the overhanging cobalt nanomagnet, acquired before it was attached to a cantilever. The magnet was $225 \pm 15\ \text{nm}$ wide, $1494 \pm 15\ \text{nm}$ long, and $79 \pm 4\ \text{nm}$ thick. There was a $4\ \text{nm}$ titanium layer under the magnet to promote adhesion to the silicon substrate, as well as an $8\ \text{nm}$ platinum capping layer to mitigate oxidation. Scale bar = $200\ \text{nm}$. (c) Top-view image of a custom-fabricated $200\ \mu\text{m}$ long cantilever drawn from the same batch as the cantilever used in this experiment. Scale bar = $20\ \mu\text{m}$.

factor and dissipation constant calculated using $Q = \tau\pi f_c$ and $\Gamma = k/(2\pi f_c Q)$, respectively. The cantilever amplitude was set to 15 nm when measuring dissipation during approach. To study cantilever frequency noise, the instantaneous frequency of the self-oscillated cantilever was determined by fitting short 4 ms segments of the digitized cantilever oscillation to a sine wave; the power spectral density of cantilever frequency fluctuations was computed from the resulting frequency versus time data. For these studies a cantilever peak-to-peak amplitude of 60 nm was chosen because it approximated the ideal amplitude for detecting a single spin at a tip-sample separation of 23 nm in a force-gradient experiment, assuming a spherical tip radius of 41 nm [17]. To determine the location of the sample surface, the tip-sample separation h was decreased until a dc deflection of the cantilever was observed. The displacement per volt of the vertical piezoelectric actuator was calibrated *via* fiber optic interferometry and the distance above this “touch point” was computed from the piezo voltage taking into account this (temperature-dependent) piezo calibration. The estimated error in h is ± 3 nm.

5.2.2 Magnetic Material Characterization

The integrity of the cantilever’s cobalt nanomagnet was analyzed *in situ* using frequency-shift cantilever magnetometry [81, 82, 89, 93, 139]; the results are shown in Section 4.4. Additional magnetic and elemental analysis of cobalt films using superconducting quantum interference device magnetometry (SQUID) and X-ray photoelectron spectroscopy (XPS) are detailed in Section 4.3. The cantilever magnetometry, SQUID magnetometry, and XPS findings indicate that the cobalt nanomagnet exhibited a saturation magnetization close to the expected value for a fully intact cobalt nanomagnet and that the unprotected nanomagnet leading edge incurred < 10 nm of oxidation.

5.2.3 Sample and Microwire Preparation

A lithographically-defined copper microwire was used to generate magnetic radiofrequency fields [12, 60]. The microwire was prepared on a silicon substrate as described in Ref. 60, but with the magnetic pillar omitted. The sample consisted of a thin film of polystyrene prepared from solution *via* spin coating. Polystyrene powder (Pressure Chemical, $M_w = 2.0 \times 10^5$, $M_w/M_n = 1.06$) was dissolved into toluene to a final concentration of 0.3 weight percent and the resulting solution was spun onto a 4 mm \times 4 mm silicon-plus-microwire substrate rotating at 6000 rpm. The high rotation speed and low viscosity resulted in a reasonably uniform film in spite of edge effects and the substrate's topographic features. The film's solvent was removed *via* air drying. Using FIB milling and SEM, the final film thickness was estimated to be 40 nm.

5.2.4 Spin Detection Protocol

Statistical fluctuations in proton magnetization were observed following the general approach of Degen *et al.* [70]. Cyclic inversions of the sample magnetization were induced by triangle-wave rf sweeps with peak-to-peak frequency modulation (FM) deviation $\Delta f_{\text{FM}} = 2$ MHz. The resulting cantilever motion was detected with a two-channel lock-in amplifier. The strength of the applied rf field was $B_1 \cong 5$ mT. The proton magnetization fluctuated with a correlation time of $\tau_m = 100$ to 150 ms; to accurately capture the induced cantilever position fluctuations, the cantilever response time was adjusted *via* feedback to be approximately 15 ms. The lock-in outputs were converted to units of force, and a spin signal was computed from the variance of the outputs using $\sigma_{\text{spin}}^2 = \sigma_x^2 - \sigma_y^2$, where σ_x^2 and σ_y^2 represent the variances of the in-phase and quadrature lock-in signals, respectively. For most data points in Figure 5.3, the spin variance signal was computed from 12.5 minutes of lock-in data per rf

frequency step. For the 117 to 126 MHz data at the three smallest tip-sample separations, $h \leq 25$ nm, the spin variance signal was computed from 16.7 minutes of lock-in data per rf frequency step.

In prior sample-on-cantilever experiments [12], optimized spin inversions were obtained using rf that was both frequency modulated (swept unidirectionally twice per cantilever cycle) and amplitude modulated (ramped to zero when the rf frequency was maximally off resonance). In this magnet-on-cantilever experiment, however, it was observed that this modulation scheme caused a parametric amplification of thermomechanical noise in one lock-in channel, yielding a false spin signal. This false variance imbalance was eliminated by operating the rf continuously and using triangle-wave frequency modulation. The triangle-wave frequency modulation, however, produced a spurious oscillation of the cantilever which in practice exhibited variations that obscured the spin signal.

Using a new spin modulation protocol COZMIC (COmpensated Zero Mean Inversion Cycles), this problem was solved by adding a small amount of amplitude modulation back into the rf so as to just cancel any spurious cantilever excitation caused by the frequency modulation. This cancelation was accomplished by measuring the mean cantilever amplitude with the lock-in amplifier and applying a sinusoidal amplitude modulation (AM) to exactly cancel the mean cantilever excitation. The frequency-modulated rf waveform was multiplied by $1 + A \cos(2\pi f_c t) + B \sin(2\pi f_c t)$, where A and B are small numbers that control the amplitude compensation. The in-phase and quadrature lock-in outputs X and Y were measured for two trials of amplitude compensation and a complex-number transfer function computed from $\chi \approx (\Delta X + i\Delta Y)/(\Delta A + i\Delta B)$. Knowing the transfer function, one can precisely predict how much amplitude modulation to apply to cancel the mean signal. After every 50 s of MRFM data collection and every time the cantilever was moved to a new location, we (1) measured the cantilever frequency, (2) computed a triangle FM waveform using

the old values of A and B for AM compensation, (3) remeasured the lock-in mean for 5 s to determine the average X and Y , (4) calculated new values for A and B using the transfer function and the measured values for X and Y , (5) updated the triangle FM waveform using the new A and B values, (6) measured the mean lock-in outputs for 5 s and calculated an updated transfer function for future use, (7) measured the MRFM signal for 50 s, and (8) repeated. This compensation scheme worked precisely and automatically.

5.3 Magnet-on-Cantilever Detection of Nuclear Magnetic Resonance

To detect nuclear magnetic resonance, the magnet-tipped cantilever was centered over the microwire and brought into close proximity with the polystyrene film coating the microwire surface (Figure 5.1). The amplitude and frequency of the rf delivered to the microwire were modulated to induce cyclic inversions of the proton spins. To avoid spurious signal, the new spin modulation protocol COZMIC was implemented, as described in Section 5.2.4. A spin variance signal was inferred by subtracting in-phase and out-of-phase force fluctuations acting on the cantilever.

In Figure 5.3 the measured spin variance signal σ_{spin}^2 (open circles) is displayed as a function of the rf center frequency f_{rf} at five tip-sample separations h ranging from 42.3 nm to 13.1 nm. For each tip-sample separation the low-frequency edge of the signal is constant at a frequency of 112 MHz, whereas the high-frequency edges increase in rf frequency as the tip is brought closer to the sample. Both of these observations are well-understood. The spin variance signal arises from protons in the sample that meet the resonance condition $f_{\text{rf}} = (\gamma_{\text{p}}/2\pi)|\mathbf{B}^{\text{ext}} + \mathbf{B}^{\text{tip}}(\mathbf{r})|$, with $\gamma_{\text{p}}/2\pi = 42.56 \text{ MHz/T}$ the gyromagnetic ratio for protons, \mathbf{B}^{ext} the applied magnetic field, and $\mathbf{B}^{\text{tip}}(\mathbf{r})$ the magnetic field generated by the cobalt

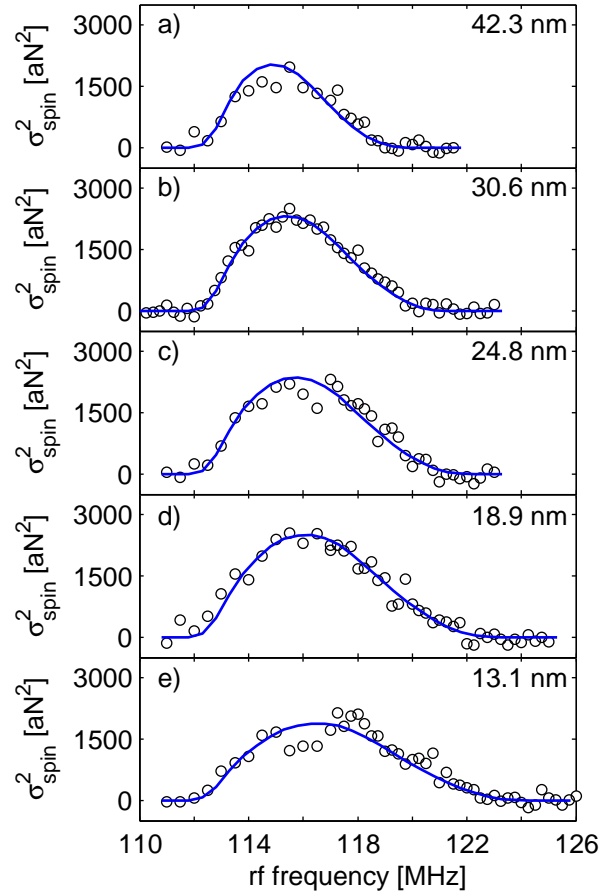


Figure 5.3: Magnetic resonance signal of protons in a 40 nm thick polystyrene film. The experimental spin variance signal σ_{spin}^2 (open circles) was obtained by measuring the spin-induced force fluctuations experienced by a cobalt nanomagnet affixed to an attonewton-sensitivity cantilever that was brought into close proximity with the film. Signal was obtained at tip-sample separations of (a) 42.3 nm, (b) 30.6 nm, (c) 24.8 nm, (d) 18.9 nm, and (e) 13.1 nm. The static field was 2.63 T and the peak-to-peak rf frequency deviation Δf_{FM} was 2 MHz. Simulated spin variance signals (blue lines) were calculated at each tip-sample separation assuming a rectangular cuboid magnet with an extraneous spacing of 51 nm (Method 1).

nanomagnet at location \mathbf{r} . The low-frequency edge of each signal shown in Figure 5.3 arises from spins far away from the tip, where the magnetic field contribution from the tip is nearly zero. For $|\mathbf{B}^{\text{ext}}| = 2.63 \text{ T}$, such “bulk” spins should meet the magnetic resonance condition at a frequency $f_1 = 2.63 \text{ T} \times 42.56 \text{ MHz/T} = 112 \text{ MHz}$, as was observed. The high-frequency edge of the signal arises from spins close to the cantilever experiencing an additional magnetic field from the cobalt nanomagnet. Due to the cobalt tip’s field gradient, the field experienced by the spins at the surface increases as the tip-sample separation is reduced.

5.4 Calculating the Tip-Field Gradient of the Cobalt Nanomagnet

The tip field and vertical tip-field gradient of the cobalt nanomagnet were estimated as a function of tip-sample separation by matching the shape of the experimental data in Figure 5.3(a-e) to simulated spin variances. In the simulations, the sample was assumed to be a 40 nm thick polystyrene film and the magnet had dimensions identical to the nanomagnet shown in Figure 5.2(b). Details of the simulation parameters are provided in the Supporting Information of Ref. 58.

Agreement between the simulations and the experimental data was obtained after considering several tip models. When simulations were conducted for a fully saturated cobalt nanomagnet, the tip field was overestimated by more than a factor of two (Figure S6 in the Supporting Information of Ref. 58). Thus, damage models had to be considered. Magnet parameters using two models were optimized to match the shape of the spin variance signal and accurately estimate the tip field. In the first model (Method 1), the magnet was assumed to have a magnetic spacing that was 51 nm larger than the measured tip-sample separation. The spin variance signals calculated using this extraneous spacing of 51 nm are overlaid

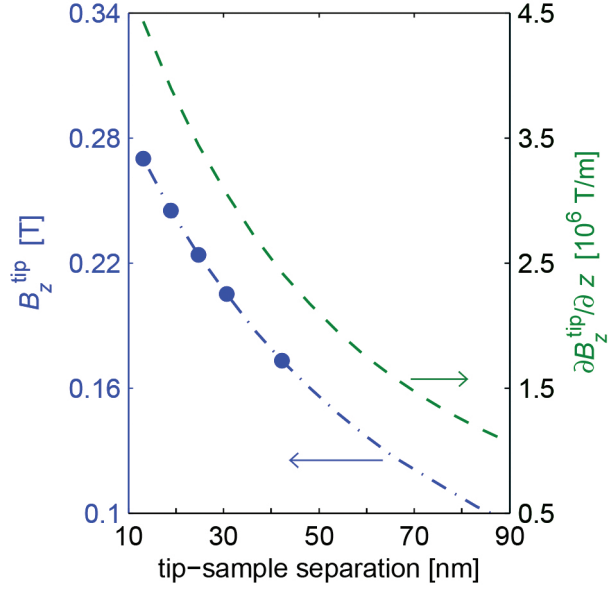


Figure 5.4: The tip field B_z^{tip} (left axis; blue) and tip-field gradient $\partial B_z^{\text{tip}}/\partial z$ (right axis; green) of the cobalt nanomagnet. As shown in Figure 5.3, a damage model for a tip with an extraneous spacing of 51 nm was used to calculate spin variance signal as a function of rf frequency. This model was used to determine B_z^{tip} as a function of tip-sample separation (blue dot-dashed line) by calculating the difference between the high-frequency and low-frequency edges of the simulated signal at 15 different spacings. The five calculated tip fields that correspond to the tip-sample separations in Figure 5.3 are shown as blue filled circles. The tip-field gradient for the cobalt nanomagnet at the same 15 tip-sample separations (green dashed line) was determined by numerically differentiating the tip fields.

with the experimental data in Figure 5.3 as the blue lines. Using Method 1, the nanomagnet's tip field B_z^{tip} was calculated as a function of tip-sample separation (Figure 5.4; blue dot-dashed line) and numerical differentiation was used to calculate the tip-field gradient $\partial B_z^{\text{tip}}/\partial z$ (Figure 5.4; green dashed line). From the tip-field gradient plot in Figure 5.4, it can be seen that at the smallest tip-sample separation of 13.1 nm the vertical tip-field gradient was calculated to be 4.4 MT m^{-1} for spins directly below the cobalt nanomagnet. In the second damage model (Method 2), the extraneous spacing was set to zero, but the saturated magnetic moment for the nanomagnet was reduced from 1.8 T to 0.69 T. Method 2 provided a quality of fit that was almost as good as for Method 1. Using Method 2, the vertical tip-field gradient was estimated as 5.4 MT m^{-1} for a tip-sample separation of 13.1 nm.

A comparison of the results obtained using Method 1 and Method 2 indicates to us that a number of tip damage scenarios could reproduce the data within experimental error but estimate somewhat different tip-field gradients. As a check, a model-free method (Method 3) for estimating the tip field and tip-field gradient was also tested as follows. The downward-sloping peak data in each curve was fit to a line, and the frequency f_h of the high-frequency edge was obtained from the x -intercept of the line. The z -component of the tip field was calculated as $B_z^{\text{tip}} = (f_h - f_l)/(\gamma_p/2\pi)$. The tip-field gradient was obtained by computing the derivative of the tip field data numerically; computing the tip-field gradient using the $h = 13.1 \text{ nm}$ and 18.9 nm data points gave the estimate $\partial B_z^{\text{tip}}/\partial z = 5.1 \text{ MT m}^{-1}$. Because of the curvature of the slope of the simulated signal, Method 3 is expected to underestimate the tip field.

In addition to the vertical tip-field gradients, the lateral gradients $\partial B_x/\partial z$ were also calculated for the nanomagnet. The lateral gradient was calculated to be 2.7 MT m^{-1} using the Method 1 tip model or 8.3 MT m^{-1} using the Method 2 tip model.

The vertical and lateral tip-field gradients shown here can be compared to the highest

reported gradients to date employed in NMR- and ESR-MRFM measurements in Table 5.1.² The cobalt nanomagnet used here has both vertical and lateral gradients that are almost an order of magnitude larger than any prior gradient achieved by affixing a magnet to the leading edge of an attonewton-sensitivity cantilever.

5.5 Dissipation and Frequency Fluctuations

The friction coefficient Γ experienced by the magnet-tipped cantilever was studied over both the (polystyrene-coated) copper microwire and the (polystyrene-coated) silicon substrate at tip-sample separations ranging from 5 to 300 nm. Measurements were conducted at 2.63 T and at zero field over both surfaces. The corresponding spectral density of force fluctuations at the cantilever frequency was calculated from the measured friction coefficient using $S_{\delta F} = 4k_B T \Gamma$ with k_B as Boltzmann's constant and $T = 5.5$ K the temperature. The resulting data are displayed in Figure 5.5. For reference, the cantilever's calculated internal friction coefficient is also shown; the cantilever's parameters far away from the surface were used to calculate the intrinsic dissipation coefficient $\Gamma = k/(2\pi f_c Q) = 2.85 \times 10^{-13}$ Ns m⁻¹, which corresponds to a thermally-limited force noise spectral density of $S_{\delta F} = 9.3$ aN Hz^{-1/2}. The dissipation over the silicon substrate remained close to the thermal limit until a separation of approximately 100 nm. In contrast, the dissipation over the microwire became surface limited at tip-sample separations below 280 nm. The dissipation over both locations was essentially independent of applied magnetic field.

The power spectral density of cantilever frequency fluctuations $S_{\delta f_c}(f)$ over both the polystyrene-coated silicon substrate and the polystyrene-coated copper microwire are plotted in Fig. 5.6. Below $f \leq 10$ Hz, $S_{\delta f_c} \propto f^{-1}$, indicative of frequency noise arising from dielectric

²Table 5.1 and Figure 5.6 reprinted with permission from the Supporting Information for J. G. Longenecker *et al.*, ACS Nano **6**, 9637 (2012). Copyright 2012, American Chemical Society.

reference	magnet location	magnet material	h [nm]	$\partial B_z^{\text{tip}}/\partial z$ [MT m ⁻¹]	$\partial B_z^{\text{tip}}/\partial x$ [MT m ⁻¹]	measurement
Method 1 ^a	on cantilever	Co	13	4.4	2.7	NMR
Method 2 ^b	on cantilever	Co	13	5.4	8.3	NMR
Ref. 53	on cantilever	SmCo ₅		0.55	0.43	ESR
Ref. 25	on cantilever	SmCo ₅		—	0.2	ESR
Ref. 54	on cantilever	SmCo ₅		0.13	—	ESR
Ref. 56	on cantilever	SmCo ₅		0.1	—	NMR
Ref. 57	on cantilever	SmCo ₅		0.25	—	ESR
Ref. 48	off cantilever	Dy	21	7.4	4.6	NMR
Ref. 12	off cantilever	Fe ₇₀ Co ₃₀	24	4.2 ^c	3.4 ^d	NMR

Table 5.1: Vertical ($\partial B_z^{\text{tip}}/\partial z$) and lateral ($\partial B_z^{\text{tip}}/\partial x$) magnetic field gradients achieved in high sensitivity magnetic resonance force microscope experiments. Tip-sample separation h is listed when available. Note that $1 \text{ G nm}^{-1} = 1 \times 10^5 \text{ T m}^{-1} = 0.1 \text{ MT m}^{-1}$.

^aNanomagnet modeled with an extraneous spacing of 51 nm.

^bNanomagnet modeled with a uniformly reduced magnetization of 0.69 T.

^cHere the revised vertical gradient estimate reported in Ref. 48 is used.

^dHere the revised lateral gradient estimate reported in Ref. 48 is used.

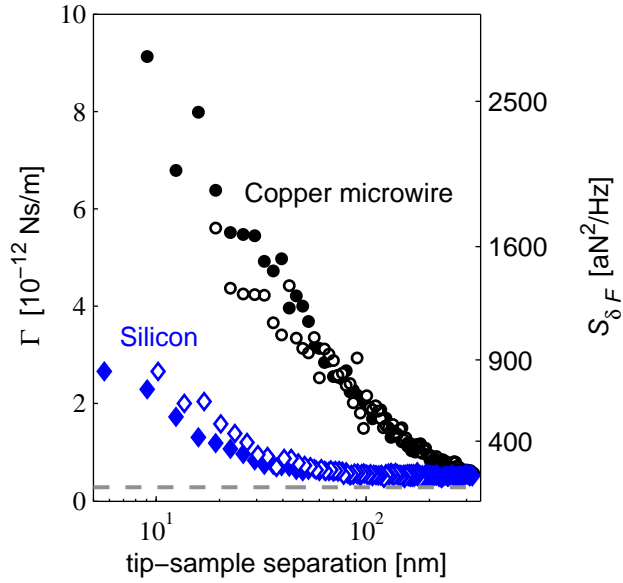


Figure 5.5: Cantilever dissipation Γ (left axis) versus tip-sample separation, and the corresponding spectral density of force fluctuations $S_{\delta F}$ at $T = 5.5$ K (right axis). Dissipation is shown for the tip centered over the copper microwire (black circles) and over the silicon substrate (blue diamonds). Measurements were conducted at $B^{\text{ext}} = 2.63$ T (closed circles and diamonds) and at zero field (open circles and diamonds). The dotted gray line is the cantilever's internal dissipation, calculated from the cantilever f_c , k , and Q measured far away from the surface.

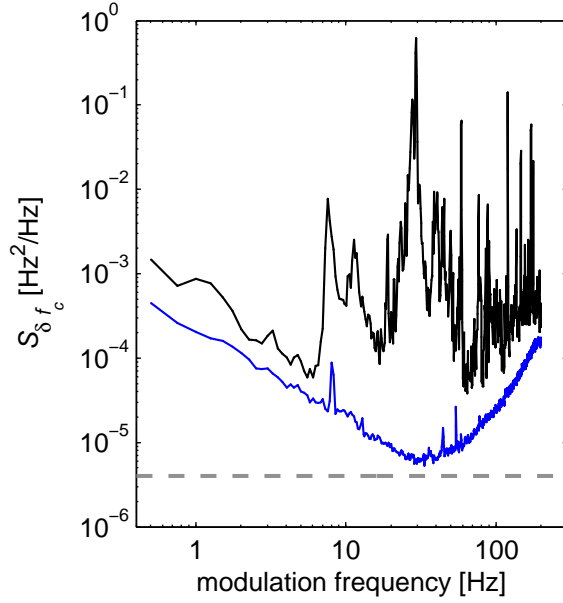


Figure 5.6: The power spectral density of the cantilever frequency fluctuations $S_{\delta f_c}$ versus modulation frequency measured over the copper microwire at 2.63 T (upper line, black) and over the silicon substrate at 0 T (lower line, blue). In both cases the surface was coated with 40 nm of polystyrene. The leading edge of the nanomagnet tip was 90 nm from the surface, and the peak-to-peak amplitude was 60 nm. The thermal noise, which was calculated to be $4.0 \times 10^{-6} \text{ Hz}^2/\text{Hz}$, is shown as the gray dashed line.

fluctuations coupling to tip charge [85, 86]. At high frequencies $f \geq 50 \text{ Hz}$, $S_{\delta f_c} \propto f^2$ as expected due to detector noise [85, 147]. Over the polystyrene-coated silicon substrate, $S_{\delta f_c}$ approaches the thermal limit at intermediate frequencies. Over the polystyrene-coated copper microwire at intermediate frequencies, in contrast, the power spectral density of cantilever frequency fluctuations is up to 10^6 larger than the thermal limit. The discreteness of the $S_{\delta f_c}$ spectrum over the microwire suggests frequency noise arising from coupling to mechanical vibrations [87].

5.6 Discussion

The data presented in Figure 5.3 and Figure 5.4 are the main results of this chapter. The successful detection of spin variance signal from protons was demonstrated in a magnet-on-cantilever MRFM experiment, and the vertical tip-field gradient of the cobalt nanomagnet was calculated to be on the order of 5 MT m^{-1} .

Method 1 and Method 2 (described in Section 5.3) provide relevant lower and upper bounds for the vertical tip-field gradient of the cobalt nanomagnet. In Method 1 the damage is modeled for the worst-case scenario, in which all damage is concentrated at the magnet-sample interface. This extraneous spacing effectively increases the tip-sample separation and would most strongly reduce the tip-field gradient experienced by spins closest to the magnet's physical leading edge. Alternately, the damage is spread evenly throughout the entire magnet in Method 2, which allows for the retention of interactions between sample spins and magnetic material as close as the measured tip-sample separation of 13.1 nm. For a tip-sample separation of 13.1 nm, Method 1 and Method 2 were used to calculate vertical tip-field gradients of 4.4 MT m^{-1} and 5.4 MT m^{-1} , respectively. As expected, the gradient estimated using Method 1 is the lower value.

To understand which, if either, of these simulated models correctly predicts the damage that led to the experimentally observed reduction in the tip field, the integrity of the cobalt material was characterized using XPS depth profiling, SQUID magnetometry, and *in situ* cantilever magnetometry. Results indicated that unprotected cobalt surfaces oxidized to a thickness of less than 10 nm, and that the rest of the cobalt remained fully intact. A simulation-free method for estimating the tip-field gradient was also used to compare to the results of Method 1 and Method 2; this method estimated that $\partial B_z^{\text{tip}}/\partial z \geq 5.1 \text{ MT m}^{-1}$. The gradient predicted by Method 1 is thus lower than expected. However, the assumption in Method 2 that the damage is uniformly spread throughout the nanomagnet is in stark

contrast with the less than 10 nm of damage expected based on the characterization measurements. Based on these findings, both of the simulation methods are likely oversimplifications of the true damage scenario. The simulation results taken together with the cobalt material characterization indicate that the discrepancy between the expected and observed tip fields may be due to a combination of (1) oxidation of all unprotected cobalt surfaces to a depth of 10 nm, (2) surface roughness on the magnet leading edge and sample film, and (3) a protrusion of the titanium underlayer past the cobalt leading edge.

While the nanomagnet’s gradient is outstanding, the dissipation experienced by the magnet-tipped cantilever is disappointingly high, particularly near the microwire. At tip-sample separations of $h \leq 20$ nm, the intrinsic force sensitivity of $9 \text{ aN Hz}^{-1/2}$ degraded to $40 \text{ aN Hz}^{-1/2}$ over the polymer-coated microwire and to $20 \text{ aN Hz}^{-1/2}$ over the polymer-coated silicon substrate. This behavior is in striking contrast with Hickman *et al.*, whose cantilever with a similarly sized nickel tip maintained a force sensitivity of $10 \text{ aN Hz}^{-1/2}$ down to $h \leq 3$ nm over a gold-coated polymer film [81]. Comparing the two experiments is instructive. In the Hickman *et al.* experiment, Γ was measured at zero field over a gold-coated polystyrene film spun on top of an ac-coupled gold halfwave microwave resonator, and the tip potential was adjusted to minimize Γ . Here, in contrast, the tip was brought over a dc-coupled copper microwire at high magnetic field, the sample covering the microwire was not metal coated, and it was not possible to adjust the tip potential to null the contact potential difference between the tip and the substrate.

There are two general dissipation mechanisms to consider: (1) tip magnetization coupling to fluctuating magnetic field gradients in the substrate, equivalent *via* the fluctuation-dissipation theorem to eddy current damping [52, 148, 149], and (2) tip charge coupling to fluctuating electric field gradients in the substrate [83, 84, 150, 151]. One might expect the eddy current damping to be stronger in a high external field where the tip is fully magnetized,

whereas Γ was instead observed to be largely field independent. However, SQUID measurements revealed the magnetic film to have significant remanence (Figure 4.8(a)), which would lead to eddy current damping even at zero field. Now consider damping arising from fluctuating electric field gradients. There are certainly stray electrostatic fields between the tip and substrate at small separations due to both differences in the overall work functions and work function inhomogeneities. Previous room-temperature dissipation measurements [17, 83, 84] have shown sizeable differences between dissipation over metal layers and over polymer films due to electrostatic/dielectric effects; these same effects may be partly responsible for the roughly four times difference between the dissipation on and off the microwire. Still, since both the silicon and the microwire were covered with the same polymer, the dominant dissipation source is suspected to be magnetic.

For a tip-sample separation of 13.1 nm and under the signal averaging conditions of Ref. 12, these magnet-tipped cantilevers are projected to achieve a resolution of 5 to 10 nm. Assuming that we are dominated by eddy current damping, a simple solution to improve the dissipation and further enhance the achievable resolution could be to increase the sample thickness or introduce a dielectric spacer between the microwire and the sample.

Acknowledgements

The data presented in this chapter was collected at the IBM Almaden Research Center in collaboration with Daniel Rugar and John Mamin. I thank both Dan and John for providing their magnetic resonance force microscope for these experiments and for their invaluable contributions to data collection and interpretation. I also thank Dan for developing the COZMIC protocol and for conducting the MRFM simulations. Additionally, I thank Charles Rettner and Mark Sherwood for assistance with polymer sample preparation. This research

was funded by the National Science Foundation through the Cornell Center for Nanoscale Systems (Grant Nos. EEC-0117770 and EEC-0646547), the National Institutes of Health (Grant No. 5R01GM-070012), the Army Research Office (Grant No. W911NF-09-C-0073), and the Army Research Office MultiUniversity Research Initiative (Grant No. W911NF-05-1-0403). This work made use of facilities in the Cornell Center for Materials Research, which is supported by the National Science Foundation Materials Research Science and Engineering Centers program (Grant No. DMR-0520404). This work also was performed in part at the Cornell NanoScale Facility, a member of the National Nanotechnology Infrastructure Network, which is supported by the National Science Foundation (Grant No. ECS-0335765).